Scientific Research Publishing

International Journal of Geosciences, 2025, 16(7), 436-463
https://www.scirp.org/journal/ijg
ISSN Online: 2156-8367
ISSN Print: 2156-8359

Deformation, Alteration and Geochemical Footprint of a Gold-Bearing Shear Zone in Metagranitoid and Metasediment, East Cameroon Goldfield

Kibong Nicoline Fontem[1,2*], Cheo Emmanuel Suh[1,3], Ralian Bryan Ngatcha[1,4], Akumbom Vishiti[5,6], Fonabe Victor Embui[2,7], Elisha Mutum Shemang[8], Ijunghi Kevin Ateh[2]

[1]Department of Geology, Mining and Environmental Science, The University of Bamenda, Bambili, Northwest Region, Cameroon
[2]Department of Mining and Mineral Engineering, National Higher Polytechnic Institute, University of Bamenda, Bambili, Northwest Region, Cameroon
[3]Economic Geology Unit, Department of Geology, University of Buea, Buea, Cameroon
[4]Department of Geology, Pan African University Life and Earth Sciences Institute (PAULESI), University of Ibadan, Ibadan, Nigeria
[5]Department of Civil Engineering, The University Institute of Technology (IUT), University of Douala, Douala, Cameroon
[6]Technology and Applied Sciences Laboratory (TASL), University of Douala, Douala, Littoral Region, Cameroon
[7]Ore Treatment Laboratory, Institute of Geological and Mining Research (IRGM), Yaoundé, Nlongkak, Cameroon
[8]Department of Earth and Environmental Sciences, Botswana International University of Science and Technology, Palapye, Botswana
Email: *fontemnicolines1@gmail.com

How to cite this paper: Fontem, K.N., Suh, C.E., Ngatcha, R.B., Vishiti, A., Embui, F.V., Shemang, E.M. and Ateh, I.K. (2025) Deformation, Alteration and Geochemical Footprint of a Gold-Bearing Shear Zone in Metagranitoid and Metasediment, East Cameroon Goldfield. *International Journal of Geosciences*, **16**, 436-463.
https://doi.org/10.4236/ijg.2025.167022

Received: May 20, 2025
Accepted: July 27, 2025
Published: July 30, 2025

Abstract

The Gankoumbol-Djouzami-Beka (GDB) area investigated in this study is part of the Central Cameroon Shear Zone (CCSZ) which is a network of anastomosing NE-SW-trending brittle-ductile mega shear. Primary gold mineralization in the area is restricted to secondary structures in the hydrothermally altered metagranitoids and metasediments pointing to a link between deformation, fluid flow and attendant mineral alteration synchronous with gold precipitation. Here, we document the spectrum of fault rocks that adorn the shear zone at the GDB area, ranging from ultramylonite/mylonite at the center of the shear zone that grades outwards through protomylonite to cataclasite at the margins. Shear sense indicators point to sinistral shear with a dominant prolate-type strain ellipsoid. The metagranitoid is subalkaline, with fault rocks characterized by alterations such as K-feldspar alteration, silicification, sericitization and sulphidation which affects the geochemistry of this altered assem-

blage. The least altered metagranitoid and fault rocks samples show LREE enrichment, depletion in HREE and a negative Eu anomaly depicting plagioclase fractionation over the various alteration categories. On the multielement variation plots, positive Rb, K, Sm, Pb, and Th anomalies and negative Nb, Sr, Ba, Ti and Zr anomalies are observed, resulting from hydrothermal alteration for the fault rocks. Gold (up to 1.8 g/t) mineralization is associated with sericitization, silicification and sulphidation. Hydrothermal alteration in fault rocks results to enrichment Mn, Cu, S, Au, Te, Fe, Bi, Ba, Mo, Mg, and depletion in Nb, Sn, As, Sb and Ga. Au-S-Cu-Mn-Te-Fe-Mo-Bi metal association constitutes a pathfinder element class reflecting gold mineralization contemporaneous with sulphidation.

Keywords

Alteration, Deformation, Gold, Cameroon

1. Introduction

Deformation is a key player as a ground preparation event for mineralization. Consequently, most deposits hosted along deformed or shear zones bear deformation imprints alongside information related to the timing of the deformation, shear sense and scale of deformation [1]-[3]. Shear zones are regions of intense deformation due to imposed regional or localized strain and favorite sites for pluton emplacement, permeable pathways for hydrothermal fluid circulation, and mineralization. Shear zones also preserve valuable structural data alongside deformation markers in orogenic belts [4] [5]. Shear zones develop in different tectonic settings, and vary in dimension and nature of fault rocks produced by heterogeneous deformation [6]. Most plutonic activities are concentrated along first and second-order large splays of strike-slip shear zones [7] such as the Central Cameroon Shear Zone. The emplacement of such plutons characterized by pervasive fluid circulation and base metal mineralization alongside gold remain poorly documented [6]. Cheng *et al.* [7] referred to such gold deposits as shear zone type gold deposits (SZTGD). A better understanding of SZTGD-style mineralization processes is pivotal in gold exploration and earth's evolutionary history. Mapping and characterization of shear zones and associated fault rocks at both macroscopic and microscopic scale is a significant exploration tool used in elucidating the relationship between deformation and mineralization [8].

The Central Cameroon Shear Zone (CCSZ) is a Pan African tectonic major transcontinental structural lineament within the Central African Fold Belt (CAFB), created by a transpressive tectonic regime, striking NE-SW with major relays as Sanaga shear zone (SSZ), Tchollire Banyo shear zone (TBSZ). It stretches from NE Brazil, across the Atlantic Ocean into the interior of Africa (**Figure 1(a)-(b)**) [9]-[13]. The tectonic evolution of the CCSZ was accompanied by oblique extensional faults (NE-SW trending) generating the Lom pull-apart basin charac-

terized by transtension and syn-tectonic magmatic activity (**Figure 1(c)**; [2] [12] [14]), with rocks bearing markers of deformation and structural features [15]. Considerable work has been done along the CCSZ precisely within the Adamawa Yadé Domain (AYD) in order to characterize the rocks and their faulted derivatives cropping out along this shear zone and also relate granitic pluton emplacement with gold mineralization [11] [16]-[19]. The wall rock, generally characterized by key hydrothermal alteration signatures such as silicification, pyritization, K-feldspar alteration, sulphidation and sericitization, is host to low-grade disseminated gold [11] [16]-[18] [20]. Significant gold concentrations occur in the hydrothermal quartz veins within the schists and the granitoids [11] [19] [21]. However, the deformation intensity/conditions, structures developed, and shear sense indicators linked to the mineralization are still poorly described.

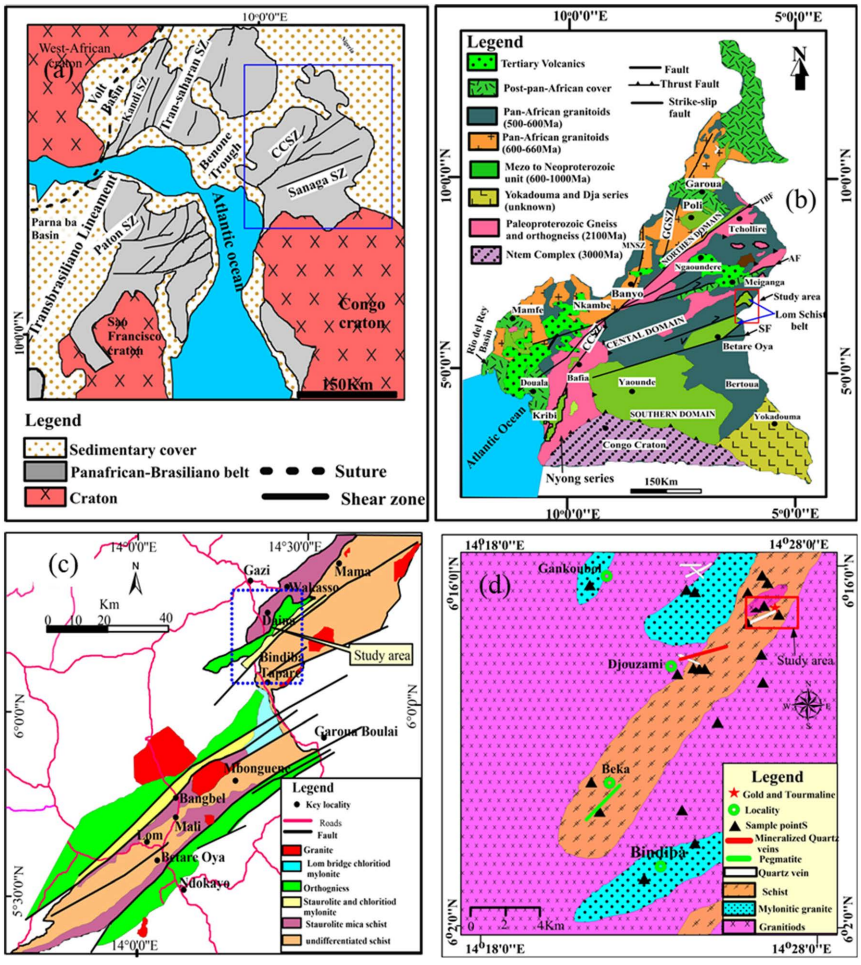

Figure 1. (a) Pan-African shear zone network in a pre-Mesozoic reconstruction of Africa and NE Brazil (modified by [15]). SZ = Shear Zone, CCSZ = Central Cameroon Shear Zone. (b) Pan African structural map of Cameroon and location of the study area (modified from Njanko *et al.*, 2010), TBF, Tcholire Banyo Fault; SF, Sanaga Fault; MNSZ, Mayo Nolti Shear Zone; GGSZ, Gode Gormaya Shear Zone; RLSZ. (c) Geologic map of the Lom pull-apart Basin with shear zones trending NE-SW [17]. (d) Geologic map of the Gankoumbol-Djouzami-Beka area (this study). The red rectangle is the insert of **Figure 2**.

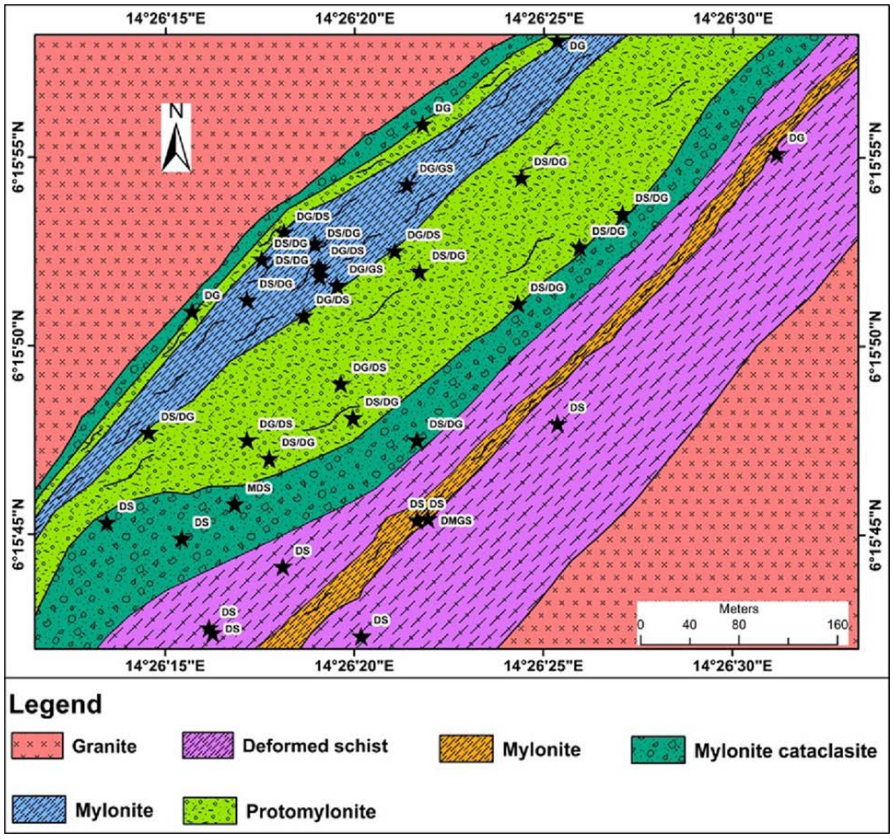

Figure 2. Simplified geologic map of Gankoumbol-Djouzami shear zone.

The Gankoumbol-Djouzami-Beka area is located in the Upper Lom Series along the CCSZ, within the AYD of the major CAFB. Gold is currently being mined from in situ weathered granitoid-metsediment saproliteby semi mechanized and artisanal miners. An integration of deformation imprints and geochemical alteration signatures in deformed facies along this shear zone can paint a better picture of Neoproterozoic gold mineralization during the tectonic evolution of the Pan African Central African Fold Belt in the Upper Lom Series.

This paper focuses on the kinematic evolution of a part of a major gold-bearing shear zone (CCSZ) in which we seek to characterize the fault rocks associated with deformation, identify shear sense indicators linked to mineralization, and apply the strain ellipsoid technique graphical representation (Flinn diagram and Rf/Ø) as a vector to interpret the deformation intensity/conditions and structures developed. We further examine the effect of deformation on the alteration mineralogy and whole rock geochemistry in a bid to provide a geochemical element association relevant to interpreting the nature of gold mineralization in the area.

2. Tectonic Setting and Regional Geology

The Central African Fold Belt (CAFB) also known as the Neoproterozoic Fold Belt of Cameroon, was formed from the amalgamation of the Congo Craton-Sao Francisco, Sahara metacraton and the West African Cratons (**Figure 1(a)**; [1] [22]

[23]), during the Pan African Orogeny. The CAFB occupies the major part of the Precambrian formation in Cameroon, bordering the northern part of the Archean-Paleoproterozoic Ntem Complex (**Figure 1(b)**), and represents the southernmost branch of the Pan-African-Braziliano Fold Belt. The CAFB is associated with multiple faults and shear zones with a general NE-SW trend, variable kinematics (early sinistral and late dextral superposition in the same NE-SW direction) and represents a major lineament beneath the crust [1] [24]. Some of which include the Central Cameroon Shear Zone (CCSZ), a NE extension of the trans-Atlantic Central African Shear Zone system (CASZ). Several subsidiary NE-trending shear zones splay off the main shear zone (CASZ), such as the Tchollire Banyo shear zone (TBSZ) to the north and the Sanaga Shear Zone (SSZ) to the south with a N30˚E to N70˚E orientation. In Cameroon, the CAFB is commonly subdivided into three main domains: (1) the North Western Cameroon Domain (NWCD) (2) the Adamawa-Yadé Domain (AYD) or Central Domain to which the study area belongs, and (3) the Yaoundé Domain (**Figure 1(b)**; [1] [10] [25]).

The AYD lies east of the Tcholliré-Banyo shear zone and extends from Cameroon (Adamawa) to the Central Africa Republic (Yadé). The AYD is characterized by strike-slip shear zones trending generally NE-SW to ENE-WSW, with Neoproterozoic metasedimentary rocks intruded by syn- to post-tectonic granitic batholiths ([16] [25] [26]; **Figure 1(b)**). The Paleoproterozoic basement units were reworked during the Pan African Orogeny [24] [25] at varying degrees of metamorphism from greenschist through amphibolite to granulite facies [10]. The rocks of the AYD have been characterized as biotite granite, K-feldspar granite, biotite metagranite, syeno-monzogranite, granodiorite, diorite and tonalite granites of High-K calc-alkaline to shoshonitic affinities [11] [16] [18] [25]. A number of shear zone-related lode gold mining sites in the vicinity of Pan-African granitoid intrusions have been described in the eastern part of the AYD [11] [16]-[20] [25]-[31]. Gold occurrences in the eastern part of Cameroon are structurally controlled by CCSZ and its relay faults, and associated with hydrothermally altered granitoids [11] [18] [19], with gold reaching a high of 103.7 ppm [20]. Sericitization, silicification, and sulphidation/ferruginization constitute the alteration assemblages within the fault rocks associated with gold mineralization in the eastern goldfields in Cameroon. The metavolcanics and Pan-African granitoids trending NE-SW are prospective zones of mineralization in eastern Cameroon, especially their contact zones with the metasediments [11] [18] [32]. The ore-forming fluids are believed to have been generated during the Pan-African orogeny and channeled along major lineaments into regional NE-trending shear zones and were responsible for gold and base-metal mineralization along these structures throughout the Pan-African mobile belt [6].

Local Geology of the Lom Basin

The Lom Series (**Figure 1(c)**) is a major pull-apart basin. It is characterized by transtensional movement [12] [25], oblique to the main shear zones (CCSZ, SFZ)

and normal faults defining its eastern and western limits. The Lom Series represents a sequence of metasedimentary and metavolcanic rocks of Pan-African age (~613 to 600 Ma, [24]), including metatuffs, volcanoclastic and sedimentary-derived schists, staurolite-garnet mica schists and quartzites with sporadic conglomerate layers [10] [12] [24] [33]. Granitoids (~635 Ma, [17]) intrude the schist and gneissic basements units, constituting the major outcrops in the Lom series [25]. The schists were metamorphosed under greenschist-facies conditions with the development of a low-pressure garnet-andalusite-staurolite regional metamorphic mineral assemblage with geochemical features attesting to derivation from argillaceous sediments [12]. Geochemical and geochronological studies carried out on the granitoids in the Lom Series reveal a crustal origin with S-type [33] and I-type geochemical signatures [17] [24]. The orientation of structures and rocks in this area follows the general N50 - N70 steeply dipping regional foliation (NE-SW trend of the CCSZ) related to D1 and D2 deformation phases during the Pan-African orogeny [12] [24]. The schist units (metasedimentary units) hosting the gold-bearing quartz veins [29] form a NE-trending corridor, dipping steeply towards the NW and subparallel to the regional foliation.

3. Sampling and Analytical Methods

3.1. Sample Collection and Preparation

The samples used in this study were collected in the upper Lom Series within a shear zone (**Figure 1(c)-(d)**). The area was systematically mapped along transects (**Figure 2**) to ensure all rock types were sampled and structural elements (foliation, lineation, shear planes, S-C fabric, boudins, folds and faults) measured. Samples spanning the spectrum from strongly altered metagranitoid- and metasediment-derived fault rocks to the least altered (fresh) fault rocks were collected for petrographic and geochemical analyses. Twenty-five (25) standard thin sections for petrographic study were prepared for all rock samples in order to decipher their mineralogy, texture, deformational fabric, as well as alteration signatures. The fault rocks in this study were classified using the classification scheme of [34]. With respect to the fault rock categorization using hydrothermal secondary minerals, the dominant mineral phase was used to name the rock purely from a petrographic perspective. All thin sections were cut in the XY and YZ structural plane (X-foliation and Z-lineation). The porphyroclast systems were analyzed using the classification scheme of [35]. The microstructural study of porphyroclast systems enabled the strain ellipsoid categories to be determined. The concept of strain ellipsoid analysis (finite strain technique) employed made use of the Rf/Ø method modified by [36] [37], and the 2D space Flinn diagram. With the Rf/Ø data, Rf = a/b; where a and b are lengths of the maximum and intermediate principal axes of the ellipsoidal marker, and Ø is the angle between the maximum principal axis and any taken reference direction (direction of principal foliation). These ratios were then plotted against the orientation of the long axis. The geometries of strain ellipsoids were also represented in 2D space using a Flinn Plot, where the ratio a

of the maximum to intermediate ellipsoid axes (a = X/Y) is plotted as ordinate and the ratio *b* of the minimum to intermediate axes (b = Y/Z) is plotted as abscissa. K represents the slope of a line from the data point to the origin at (1,1), so that K = a − 1/b − 1 with a = x/y and b = y/z. The modified Flinn Plot by [36] provides a more even distribution of points with increase in deformation, making data interpretation less difficult. Foliations, lineation and poles of the collected structural data were plotted in the lower hemisphere of Schmidt net diagrams following conventional techniques [38].

3.2. Whole Rock Geochemical Analytical Methods

A total of 15 samples were crushed, pulverized to below 75 μm mesh and analyzed for major and trace elements (Au inclusive) at Bureau Veritas Mineral (BVM) Laboratory Vancouver, Canada. These samples were decomposed by lithium tetraborate/lithium metaborate/sodium nitrate ($Li_2B_4O_7/LiBO_2/NaNO_3$) fusion discs using code XF 700, and whole rock major concentrations for the fault rocks, meta-granite and metasediment were determined by X-ray fluorescence spectrometry (XRF). The trace and Rare Earth Elements were analyzed by inductively coupled plasma-mass spectrometry (ICP-MS), after aqua regia extraction and total digestion (code, AQ250_EXT_REE), while Au concentration was determined by fire assay with a Ni-S finish. Loss on Ignition (LOI) was determined by heating the powdered samples at 850 °C for 3h. Accuracy and precision are better than 5% RSD (% relative standard deviation). Geostandards used in the analyses are STD OREAS184, STD SY-3(D), STD LOI471, STD LOI472, STD BVGEO01, STD OREAS262 and international rock standards, such as OREAS184 (4-acid), SdAR-M2 (USGS).

4. Results

4.1. Lithological Description and Structural Features

The rock types encountered in the Gankoumbol-Djouzami-Beka shear zone consist of granites, schists, metamorphosed unaltered rocks (metagranitoid and metasediments) and the faulted derivatives of the metagranitoid, showing varying intensity of deformation and hydrothermal alteration. The fault rocks grade outward from ultramylonite, at the center of the shear zone through mylonite, protomylonite, to cataclasite at the margins of the shear zone (**Figure 2**). Strain compartmentalization with strongly ductile deformed samples at the center of the shear zone, grading out to brittle zone. Shearing is accompanied by progressive grain size reduction, strong mineral lineation and foliation as strain increases in the fault rocks towards the center of the shear zone (**Figures 3(a)-(c)**). The planes of schistosity are impregnated with quartz injections, healing the S1 foliations in mylonite (**Figure 3(b)**). These rocks are transected by quartz veins and fractures of different generations at the outcrop scale. The NW-SE second generation veins/fractures displace the dominant NE-SE structures in both dextral and sinistral manner (**Figures 3(d)-(e)**). Shear sense indicators and the deformation con-

ditions also vary across the shear zone, with ultramylonites, mylonites and protomylonites presenting well-developed mylonitic foliation defined by preferred mineral orientation with a NE-SW trend (Figure 3(a) and Figure 3(f)). Faults, fractures, microfolds and S-C fabric constituted the dominant shear sense indicators in the study area both at the microscopic and microscopic scale (Figure 3 and Figure 4). These shear sense indicators depicted both dextral and sinistral sense of shearing (Figures 3(d)-(e)). The S2 foliations are transformed to S3 foliations by microfolds in ultramylonite with increase in deformation strain (Figure 3(f)). These fault rocks outcrop define a N10E-N70E (NNE-SSW to NE-SW) trend which is aligned parallel to the dominant NE-SW trend of the CCSZ lineament.

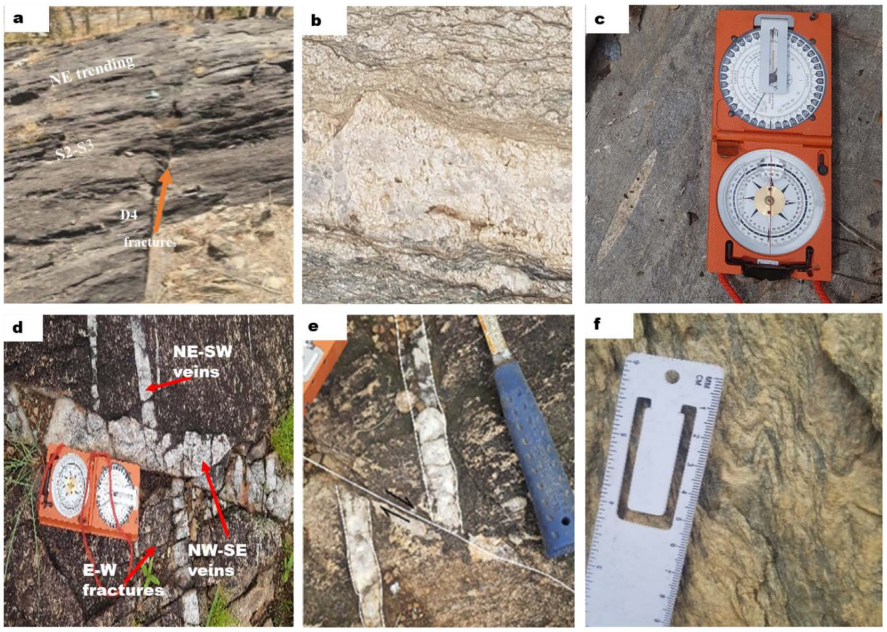

Figure 3. Feld photographs depicting the different shear sense indicators and structures. (a) Fine to medium-grained schist with Visible foliations and NW-SE oriented fractures. (b) Quartzo-feldspathic Veins. (c) Mineral lineation defined by elongated quartz. (d) Sinistral sense of shearing in schist depicting a D4 NW-SE fractures displacing NE SW veins. (e) Sinistral sense of movement in fault rocks. (f) Microfolds transposing S1 foliations to S2 foliations in sheared schist depicting ductile deformation.

1. Least Altered Metagranitoid and Metasediments

The least altered metagranitoid presents very limited features of deformation. They are coarse-grained and leucocratic (Figure 4(a)) with biotite, feldspars (microcline, orthoclase), quartz and minor muscovite as dominant minerals (Figures 4(b)-(c)). Microcline displays cross-hatch twinning with quartz, biotite and muscovite inclusions. The least altered metasediments, on the other hand, are fine to medium-grained, dark gray and mesocratic with foliations healed with quartz (Figures 4(d)-(f)). The mineralogical make-up consists of quartz, muscovite, biotite with minor feldspars. Silicification is the main alteration in the rock (Figure 4(f)).

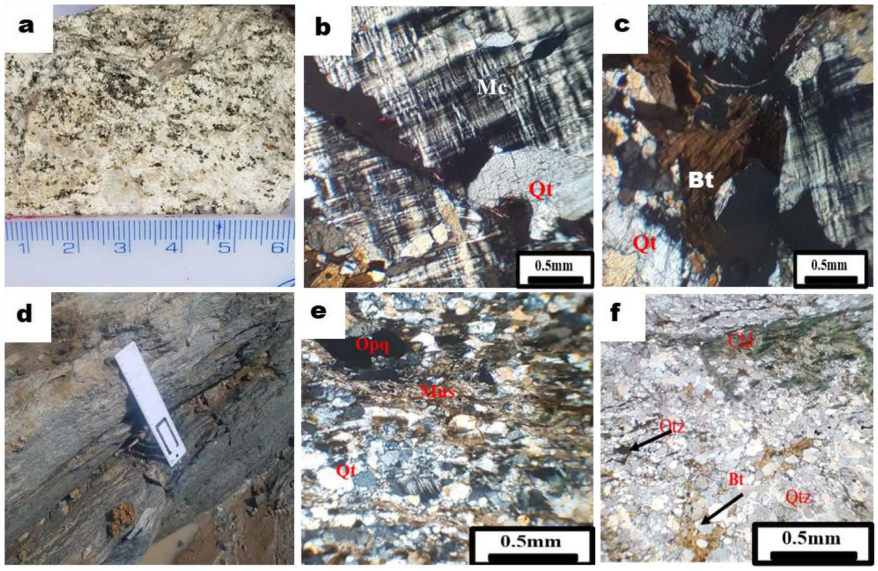

Figure 4. Hand specimens and photomicrographs of the leucocratic least deformed metagranitoidand metaschist. (a) hand specimen of the least deformed metagranitoid. (b) Large microcline crystals with quartz inclusion, and exhibiting tartan twinning. (c) Biotite flakes in association with microcline. (d) Hand specimen of the basement metaschist. (e) Metasediment with pyrite associated with the mylonitic foliation. (f) Chlorite bands defining the mylonitic foliation in the basement metasediment.

2. Fault rocks (ultramylonite, mylonite, protomylonite and cataclasite)

These rocks range from very fine-grained ultramylonite to weakly foliated cataclasites at the margins of the shear zone (Figure 2 and Figure 5). Under the microscope, the mylonitic fabric is defined by a strong foliation depicted by preferred orientation of minerals in the ultramylonite (Figures 5(b)-(c)), and alternating bands of microlithons with cleavage domains in the protomylonite (Figures 5(e)-(f)). Its mineralogy consists of quartz and feldspars porphyroclasts, sericite and muscovite. The sericite content of these fault rocks is remarkably high as it develops at the expense of feldspar (Figures 5(e)-(f)). Grain size reduction is prominent with the development of fine-grained quartz seams sub-parallel to sericite mosaics that 'flow' around the porhyroclasts (Figures 5(e)-(f)). Sericite occurs in association with disseminated sulphide minerals, defining NE-SW veins/veinlets (Figure 5(b), Figures 6(b)-(c)). They also occur in patches and fractures in feldspars in the cataclasite zone (Figures 5(e)-(f)). K-feldspar alteration cuts across the shear zone, but dominant towards shear zone margins, and gives a pinkish color to the rock (Figure 6(d)). At the mylonitic zones where strain rate is high, K-feldspars occur as porphyroclast resulting from intense deformation and shearing towards the center of the shear zone (Figure 5(f) and Figure 6(b)). K-feldspars also depict evidence of syn-to-post magmatic deformation (Figure 6(f)).

Compositional layering is observed in protomylonite, with alternation of fine-grained chlorite/muscovite/sericite bands, and dynamically recrystallized quartz bands (Figure 6(c)). Sulphidation decreases with increasing K-feldspar alteration, associated with sericite mosaic (sericitization) and quartz seams (silicification)

within the shear zone, but more pronounced within the protomylonitic and cataclastic zones, as euhedral to subhedral pyrite crystals (Figures 6(b)-(c)). Silicification occurs as dynamically recrystallized quartz sub-grains, with quartz defining porphyroclast towards the mylonite zone (Figure 5(e), Figure 6(c) and Figure 6(e)). Silicification cuts across the shear zone, and constitutes the ground mass mantling the feldspars in the fault rocks. Silicification bands alternate with sulphidation bands towards center of shear zone (Figure 6(c)). Within the ultramylonite zone, quartz occurs as elongated ribbons defining lineation (Figure 5(a)). Microfolds of muscovite transform S2 foliations to S3 foliations in ultramylonite depicting ductile deformation (Figure 5(c)).

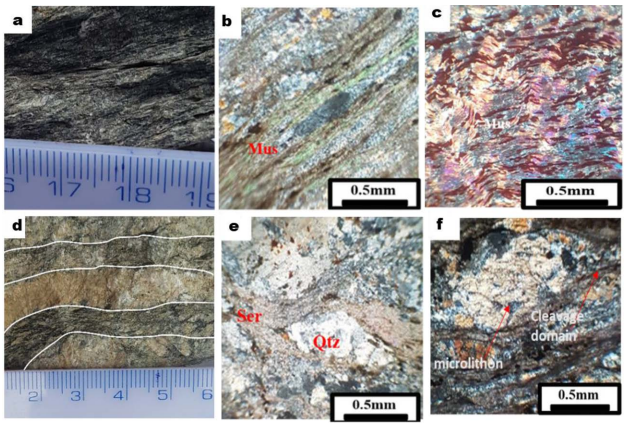

Figure 5. Photomicrographs of the fault rocks and associated hydrotherma lalteration. (a) Mylonite with strong mineral foliation defined by platy muscovite flakes. (b) Space cleavage in ultramylonite with mineral lineation. (c) Folded muscovite band in ultramylonite depicting duictile deformation. (d) Metasediments with fractures healed with quartz. (e) Anastomosing mylonitic foliation defined by lensoid microlithon and cleavage domain in the mylonite. (f) Mylonite with cleavage domain and microlithon.

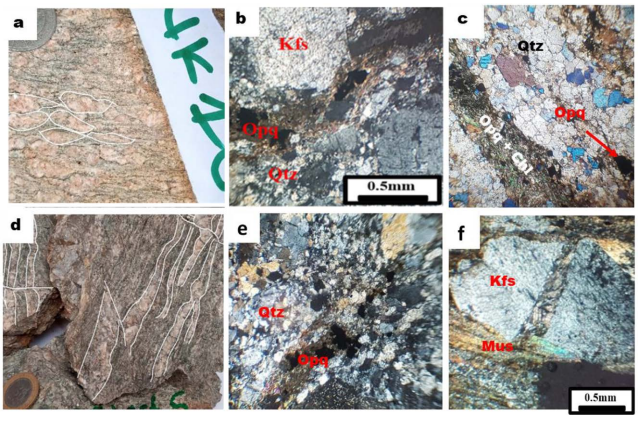

Figure 6. Photomicrographs of the fault rocks and associated hydrotherma lalteration. (a) Mylonite with strong mineral foliation defined by platy muscovite flakes. (b) Space cleavage in ultramylonite with mineral lineation. (c) Folded muscovite band in ultramylonite depicting duictile deformation. (d) Metasediments with fractures healed with quartz. (e) Anastomosing mylonitic foliation defined by lensoid microlithon and cleavage domain in the mylonite. (f) Mylonite with cleavage domain and microlithon.

3. Microshear sense indicators and porphyroclast system

Microscopically, quartz and feldspar sigmoidal porphyroclast ("σ"), micafish, S-C fabric, microfolds and faults define the dominant shear sense indicators from the protomylonite to ultramylonite at the center of the shear zone (Figures 7(a)-(f)). Winged and non-winged porphyroclast systems are observed, with varying sizes and shape. The porphyroclast systems have elliptical grain shapes with long axes aligned subparallel to the main NE-SW foliation resulting from vertical stretching during deformation (Figures 7(a)-(b) and Figure 7(f)). The "σ" porphyroclast and snowball structures depict both sinistral and dextral sense of shearing (Figure 4(a) and Figure 4(c)). The finite strain ellipsoid analysis made used of quartz and K-feldspars porphyroclast with long axes inclined or parallel to the principal foliation. From the plots the samples show dominant prolate strain ellipsoids with constriction type of deformation (Figures 8(a)-(b)). Relics of oblate strain ellipsoids defining flattening type deformation were also observed in both Rf/Ø method and the 2D space Flinn diagram. The two methods employed yielded similar trends.

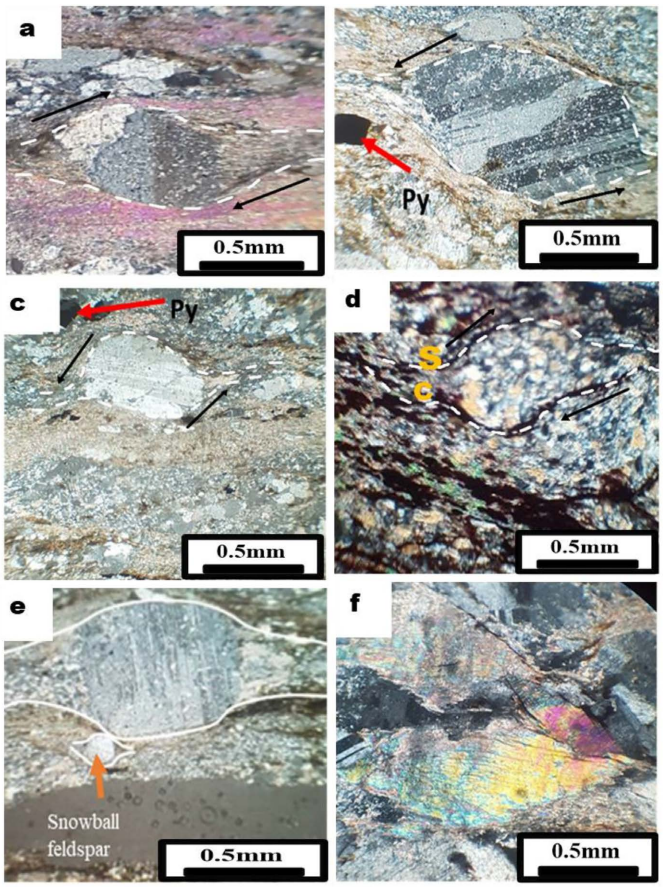

Figure 7. Photomicrographs of microscopic shear senseindicators depicting both sinistral anddextral senseofshearinthestudyarea. (a) (d) Dextral shear sense indicators associated with sulphidation (pyrite); (b) (c) Sinistral shear senseindicators associated with sulphidation (pyrite); (f) Micafish in fault rock depicting a dextral sense of shear; (e) Snow ball structures associated with shear sense indioators.

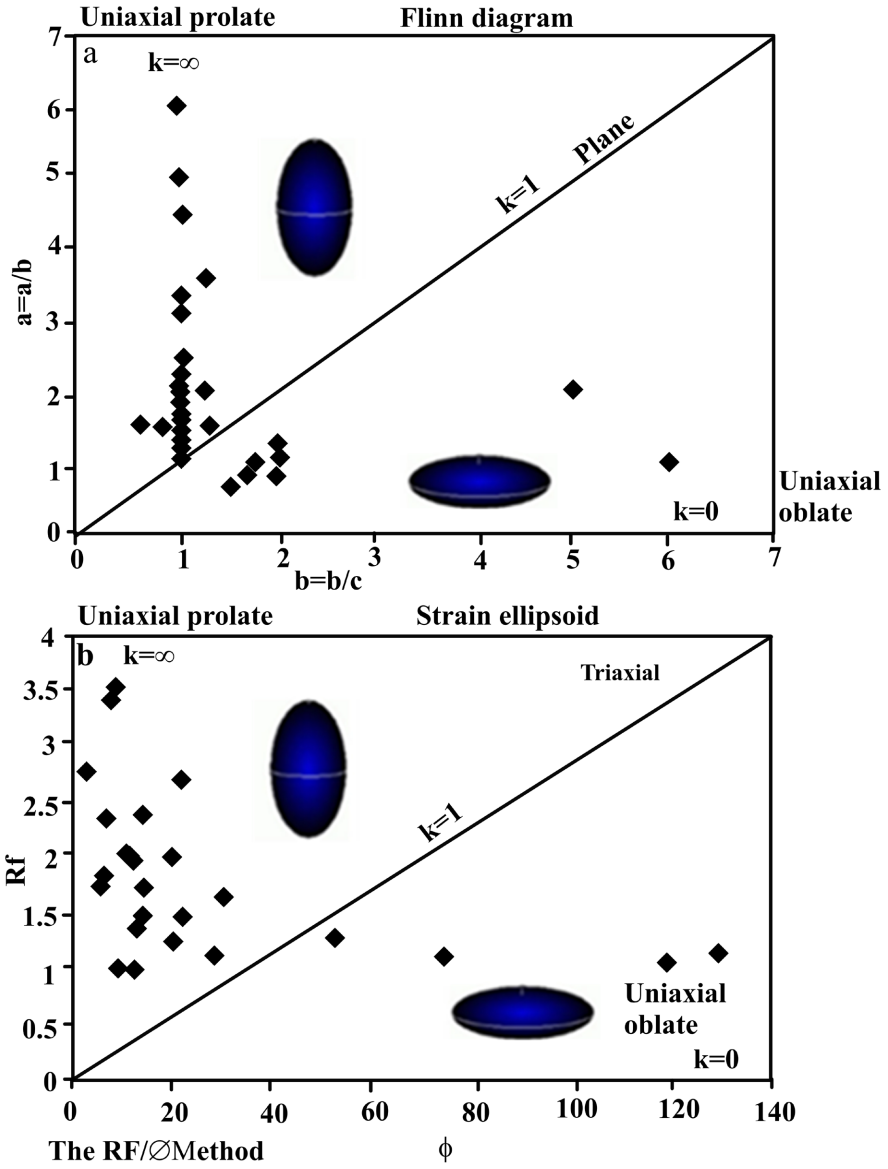

Figure 8. (a) Flinn Diagram; (b) The Rf/Q method depicting dominance of prolate strain in the studied shear zone.

4.2. Whole Rock Geochemistry of the Gankoumbol-Djouzami-Beka Metagranitoids, Fault Rocks and Metasediments

The major, trace, and rare earth elements (REE) geochemistry of the analyzed fault rocks, meta-granite and metasediment rocks are presented in Table 1. The fault rocks are grouped into four (4) variably altered categories based on hydrothermal alteration (sericitized, silicified, sulphidized and K-feldspar altered-fault rock). The analyzed metagranitoid samples are subalkaline and plot in the granite and granodiorite fields on the TAS classification diagram (Figure 9(a); [39]). They show per-alkaline high K-calc-alkaline character (Figures 9(b)-(c) [40] [41]) and plot in the field of volcanic arc granitoid (Figure 9(d)) on the geotectonic discrimination diagram of [42].

Table 1. Whole rock major (wt.%) trace and rare earth elements (ppm) composition of the Gankoumbol-Djouzami-Beka area. The various fault rocks and their alteration signatures are identified as well as the least altered metagranite and schist.

	Fault Rock												Matagranite		Metasediment
	Fault rock Sericitized (Sericitization)					Fault rock Silicified (Silicification)			Fault rock Sulphidized		Fault rock K-Feldspar Alteration		K-Feldspar		Silicification
Rock Samples	CMR_ B31	CMR-B32	CMR-B33	CMR-B41	CMR-B43	CMR-B42	CMR-B34	CMR-B35	CMR-B36	CMR-B38	CMR-B39	CMR-B44	CMR-B40	CMR-B45	CMR_B37
SiO_2	65.3	63.11	68.97	71.64	67.27	66.08	79.83	74.76	74.04	64.88	74.96	73.62	71.46	71.71	78.88
Al_2O_3	14.41	15.01	14.83	14.58	14.53	14.39	11.22	13.92	14.64	14.75	12.69	13.5	14.54	15.2	10.35
Fe_2O_3	4.64	4.49	3.37	3.37	3.96	4.33	1.46	1.46	1.68	6.09	2.15	2.3	2.56	2.53	1.31
MgO	1.97	1.32	1.25	1.21	1.46	1.5	0.05	0.14	0.17	2.16	0.29	0.42	0.44	0.57	0.04
CaO	2.99	2.99	1.13	0.23	2.34	2.88	0.13	0.78	0.67	1.16	0.77	0.5	2.19	2.18	0.25
Na_2O	4.16	4.86	4.73	4.57	4.25	3.25	4.98	4.01	3.86	4.21	3.5	3.54	3.67	3.66	3.12
K_2O	2.73	2.92	2.97	3.27	3.06	3.65	1.87	4.03	4.07	2.59	5.09	5.42	3.63	3.94	4.2
TiO_2	0.49	0.53	0.42	0.42	0.44	0.47	0.07	0.11	0.11	0.59	0.29	0.28	0.26	0.31	0.1
P_2O_5	0.15	0.15	0.13	0.13	0.13	0.15	0.06	0.06	0.07	0.14	0.05	0.05	0.09	0.08	0.01
MnO	0.13	0.14	0.08	0.06	0.11	0.17	0.09	0.12	0.09	0.33	0.04	0.06	0.05	0.03	0.04
Cr_2O_3	0.01	0.01	0.01	0.01	0.01	0.01	0.01	0.01	0.01	0.01	0.01	0.01	0.01	0.01	0.01
SO_3	0.002	0.002	0.002	0.002	0.002	0.002	0.002	0.002	0.002	1.352	0.002	0.002	0.002	0.002	0.002
LOI	3.2	4.4	1.8	1.1	3	3.6	0.3	1.3	1.2	2.3	0.4	0.4	1.4	0.4	0.2
Total	100.182	99.932	99.69	100.592	100.562	100.482	100.072	100.702	100.61	100.56	100.24	100.102	100.302	100.622	98.512
Ag	12	43	50	15	39	9	178	54	148	60	11	46	42	33	13
Au	0.2	0.2	0.2	0.2	0.3	0.2	0.6	0.2	0.3	1.8	0.2	0.2	0.2	0.2	0.2
As	0.8	0.9	0.5	0.6	1.1	1.2	1	1.7	0.7	1.8	0.3	0.4	1.8	1.8	0.3
Al	1.4	0.58	0.82	0.86	0.95	1.03	0.24	0.26	0.36	1.5	0.38	0.53	0.77	0.99	0.24
Ba	101.6	78.7	124.9	157.2	85.1	127.2	73.5	77.2	123.9	174.3	28.9	48.3	62.2	60.2	10.4
Bi	0.16	0.27	0.23	0.33	0.06	0.05	1.34	0.34	0.48	0.46	0.08	0.14	0.15	0.12	0.2
B	20	20	20	20	20	20	20	20	20	20	20	20	20	20	20
Be	0.3	0.3	0.3	0.5	0.2	0.4	0.2	0.3	0.5	0.4	0.6	0.4	0.5	0.2	1
Ca	1.88	2	0.73	0.12	1.57	1.98	0.05	0.5	0.41	0.3	0.34	0.07	0.76	0.11	0.14
Cd	0.06	0.09	0.04	0.01	0.07	0.15	0.03	0.06	0.12	0.1	0.06	0.05	0.08	0.02	0.01
Co	9	5.4	3	5.7	6.8	7.3	0.7	0.3	0.4	16.8	1.7	2.5	2.7	4.3	0.3
Cr	10	11.6	6.3	8.9	11.5	6.9	14.4	9.8	17	15.5	11.3	18.2	7.9	15	9.3
Cs	5.14	0.99	2.17	2.78	0.57	4.49	0.17	0.4	0.37	2.67	0.3	0.78	8.92	6.26	0.12
Cu	1.43	2.62	2.91	6.18	9.75	3.2	7.91	1.82	2.52	56.94	2.61	34.43	1.15	2.1	2
Fe	2.5	2.13	1.48	1.62	2.17	1.99	0.91	0.64	0.64	3.61	1.25	1.42	1.55	1.79	0.83
Ga	4.1	1.6	2.8	2.8	4.6	2.8	0.5	0.6	0.8	5.3	2.2	2.2	4.9	6	1.3
Ge	0.1	0.1	0.1	0.1	0.1	0.1	0.1	0.1	0.1	0.1	0.1	0.1	0.1	0.1	0.1
Hf	0.41	0.27	0.29	0.35	0.14	0.24	0.17	0.2	0.18	0.3	0.76	0.36	0.55	0.48	1.47

Continued

Hg	5	5	5	5	5	5	5	5	5	5	5	5	5	5	5
In	0.02	0.02	0.02	0.02	0.02	0.02	0.02	0.02	0.02	0.02	0.02	0.02	0.02	0.04	0.02
Li	22.6	10.6	10.9	9.9	16.1	15.3	0.4	1.4	1	10	2.6	6.5	46.2	54.3	1
Mo	1.14	1.89	0.95	1.44	1.63	1.26	3.48	2.28	6.6	2.25	2.11	5.25	0.98	1.5	2.5
Mg	0.97	0.52	0.46	0.46	0.7	0.57	0.01	0.01	0.01	1.08	0.13	0.21	0.2	0.32	0.01
Mn	834	983	536	400	754	1213	696	869	649	2456	270	303	285	238	160
Ni	3.5	3.6	1.6	2.5	3	2.3	2.8	1.8	2.9	10.1	2.7	3.8	2.6	4.6	1.7
Na	0.054	0.057	0.046	0.047	0.04	0.035	0.077	0.046	0.053	0.043	0.042	0.062	0.04	0.06	0.05
Nb	0.04	0.07	0.02	0.05	0.03	0.08	0.2	0.14	0.16	0.15	4.09	0.55	0.7	0.31	10.75
P	0.06	0.058	0.055	0.053	0.054	0.062	0.022	0.019	0.022	0.058	0.019	0.02	0.035	0.031	0.001
Pb	2.99	7.59	5.29	5.65	3.68	6.2	13.59	12.42	7.55	6.5	7.64	6.75	6.95	2.92	11.24
Rb	50.6	22.4	33.8	42.5	11.1	57.1	5	10.8	13.7	54.5	15.1	39.2	66.7	80.3	14.9
Re	1	1	1	1	1	1	1	1	1	2	1	1	1	1	1
Sr	38.6	100.7	40.3	8.2	56.1	64.3	9.4	16.1	15.1	30.6	14.1	6.9	8.7	8.3	1.6
Sb	0.44	0.28	0.3	0.37	0.36	0.49	0.09	0.11	0.06	0.26	0.12	0.13	0.39	0.08	0.07
Sc	3.1	2	1.7	1.7	3.1	1.8	0.6	0.4	0.4	5.3	2.1	1.5	2	2.8	0.4
S	0.02	0.02	0.02	0.02	0.02	0.02	0.02	0.02	0.02	0.59	0.02	0.02	0.02	0.02	0.02
Se	0.2	0.1	0.1	0.1	0.1	0.1	0.1	0.1	0.1	0.3	0.1	0.1	0.1	0.1	0.1
Sn	0.4	0.2	0.3	0.3	0.3	0.2	0.2	0.3	0.4	0.6	1.7	0.5	1.9	2.9	0.9
Ta	0.05	0.05	0.05	0.05	0.05	0.05	0.05	0.05	0.05	0.05	0.05	0.05	0.05	0.05	0.05
Tl	0.31	0.13	0.19	0.24	0.05	0.33	0.04	0.05	0.06	0.52	0.08	0.15	0.42	0.45	0.05
U	0.9	1.4	0.8	1.1	0.9	0.8	0.8	1	0.9	1.8	1.5	3.1	3.7	3.1	2.6
V	23	14	7	8	22	15	1	1	1	50	7	10	15	21	1
W	0.2	0.6	0.2	0.1	0.1	2.1	0.2	0.3	0.3	0.2	0.3	0.3	1.4	0.1	0.8
Y	16.05	7.62	8.95	9.68	14.43	12.62	2.75	3.86	5.1	18.62	38.66	11.14	43.87	4.02	23.47
Zn	51.2	26.8	44.7	48.1	55.5	59.1	14.8	20.3	15	38.9	31.9	50.3	68.1	72.4	26
Zr	15.6	9.7	10.8	13.2	4.6	7.5	4.5	5.8	4.4	8.6	19.5	10.4	15.6	12.9	31.4
La	15.2	19.9	21.6	15.5	17.3	22.4	14.6	23	28.7	19.7	57.2	27.9	25.6	12.2	23.7
Ce	30.7	40	40.9	58.7	35.8	35	31.2	48.5	59.2	40.4	103.2	102.5	43.2	45.8	89.8
Sm	3.15	3.41	3.93	3.29	3.48	4.27	2.41	3.71	4.48	3.73	6.64	3.32	4.68	2.44	3.79
Eu	0.71	0.73	0.72	0.6	0.77	0.92	0.51	0.67	0.82	0.82	0.64	0.46	0.58	0.14	0.04
Gd	3.15	2.55	2.94	2.62	3.12	3.59	1.61	2.41	2.91	3.49	5.96	2.18	5.83	1.57	3.02
Tb	0.45	0.31	0.34	0.36	0.42	0.44	0.17	0.25	0.31	0.52	0.91	0.33	0.74	0.18	0.59
Dy	2.69	1.59	1.76	1.97	2.46	2.34	0.73	1.06	1.31	3.26	5.84	2.06	4.24	0.91	4.29
Ho	0.51	0.27	0.3	0.36	0.48	0.42	0.1	0.15	0.18	0.64	1.21	0.39	0.86	0.14	0.92
Er	1.43	0.74	0.82	1.01	1.43	1.23	0.23	0.34	0.43	1.84	3.73	1.18	2.27	0.36	3.07
Tm	0.2	0.11	0.11	0.14	0.21	0.18	0.03	0.05	0.06	0.26	0.55	0.18	0.27	0.04	0.52

Continued

Yb	1.33	0.73	0.76	0.95	1.41	1.32	0.19	0.33	0.41	1.67	3.61	1.25	1.4	0.25	3.83
Lu	0.19	0.11	0.11	0.14	0.21	0.21	0.03	0.05	0.06	0.24	0.54	0.18	0.2	0.03	0.55
Pd	10	10	10	10	10	10	10	10	10	10	10	10	10	10	10
Pt	2	2	2	2	2	2	2	2	2	2	2	2	2	2	2
$Na_2O + K_2O$	7.70	6.89	7.32	7.78	7.31	6.90	6.85	8.04	7.93	6.80	8.59	8.96	7.84	7.60	7.30
K_2O/Na_2O	0.63	0.66	1.35	0.60	0.72	1.12	0.38	1.00	1.05	0.62	1.45	1.53	0.72	1.08	0.99
A/CNK (ASI)	1.68	1.46	1.37	1.39	1.51	1.47	1.61	1.58	1.70	1.85	1.36	1.43	1.81	1.55	1.53
A/NK	1.93	2.09	1.41	1.93	1.99	2.09	1.64	1.73	1.85	2.17	1.48	1.51	1.86	2.00	1.99
CIA	63.85	60.57	57.86	59.37	61.19	60.79	62.33	61.76	63.63	66.31	57.99	59.23	65.63	61.50	61.27
LaN/YbN	7.71	18.38	19.16	11.00	8.27	11.44	51.81	46.99	47.19	7.95	10.68	15.05	12.33	32.90	4.17
LaN/SmN	3.04	3.67	3.46	2.96	3.13	3.30	3.81	3.90	4.03	3.32	5.42	5.29	3.44	3.15	3.93
CeN/YbN	5.97	14.17	13.92	15.98	6.57	6.86	42.48	38.02	37.35	6.26	7.39	21.21	7.98	47.39	6.06
CeN/SmN	2.35	2.83	2.51	4.31	2.48	1.98	3.12	3.15	3.19	2.61	3.75	7.45	2.23	4.53	5.72
GdN/YbN	1.19	2.82	3.25	2.22	1.79	2.19	6.84	5.89	5.73	1.69	1.33	1.41	3.36	5.05	0.64
ΣREE	78.13	92.41	99.84	105.7	88.25	98.78	68.2	105.98	129.97	99.5	241.2	168.25	116.74	79.32	157.82
Eu*Eu	0.69	0.76	0.65	0.62	0.71	0.72	0.79	0.69	0.69	0.69	0.31	0.52	0.34	0.22	0.04

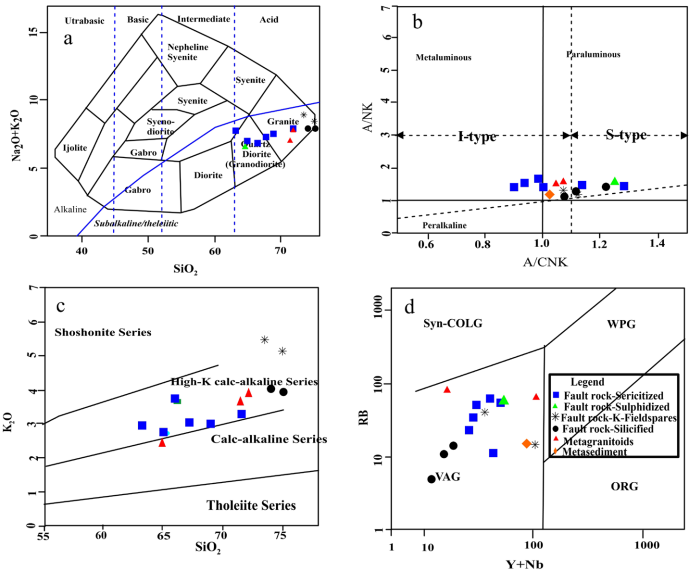

Figure 9. (a) Whole rock geochemical classification plots of the metagranites, metasediments, and faultnocks. (a) SiO_2 vs $Na_2O + K_2O$ (TAS) diagram of [32]; (b) A/CNK (Ahuminum Sattiration Index) versus A/NK diagram of [33]. Samples are weakly metaluminous to peraluminous, L-type to S-type (ASI = 1.3 - 1.8); (c) K_2O vs SiO_2 diagram of [34], the rocks plot in the high-k calc-alkaline fields; (d) Tectonic discrimination diagram of [35], granitoids plot in the field of VAG (Field symbols; VAG: Voloanic Arc Granitoids); Syn-COLG, syn-collisional granitoid; WPG, within-plate granitoid; ORG, oceanic ridge granitoid.

4.2.1. Major Element Composition

1. Least altered rocks

Least altered metagranitoid (CMRB-40, CMR-B45) display a silica content that vary between 71.46 and71.71 wt.%, high Al_2O_3 (14.54 wt.% - 15.2 wt.%), K_2O (3.63 wt.% - 3.94 wt.%) and $K_2O + Na_2O$ contents that range from 7.6 to 7.84wt.%), moderate CaO (2.18 wt.% - 2.19 wt.%), and Na_2O content from 3.66 to3.67wt.%. They are characterized by low P_2O_5 (0.05 wt.% - 0.15 wt.%), FeOt (2.53 wt.% - 2.56wt.%), MgO (0.44 wt.% - 0.57 wt.%), TiO_2 (0.26 wt.% - 0.31wt.%) and MnO (0.03 wt.% - 0,05 wt.%), K_2O/Na_2O ratios (0.72 wt.% - 1.08 wt.%). The LOI value varies between 1.4 and 0.4 wt.% (Table 1).

2. Fault rocks (altered samples)

The fault rocks in this study are grouped into four (4) categories based on hydrothermal alteration. The hydrothermal alteration includes: sericitization, silicification, sulphidation and K-feldspar alteration (Figures 10(a)-(h)). These altered samples represent the shear zone studied. The analyzed Fault rock-sericitized samples are characterized by a low to moderate silica content (63.11 wt.% - 71.64 wt.%), high Al_2O_3 (14.41 wt.% - 15.01 wt.%), LOI values from 1.1 wt.% - 4.4 wt.%, slight increase in FeOt (2.56 wt.% - 4.64 wt.%), low K_2O (2.73 wt.% - 3.65 wt.%), CaO (0.23 wt.% - 2.99 wt.%) and high $K_2O + Na_2O$ (6.89 wt.% - 7.84 wt.%). The Na_2O values range from 3.25 to 4.86 wt.%. The concentration of TiO_2 (0.26 wt.% - 0.49 wt.%), MgO (0.44 wt.% - 1.97 wt.%), MnO (0.06 wt.% - 0.17 wt.%), P_2O_5 (0.09 wt.% - 0.15 wt.%), and K_2O/Na_2O ratios (0.60 wt.% - 1.35wt.%) are generally low.

The fault rock-silicified samples are characterized by high silica content (74.04 wt.% - 79.83 wt.%), low to moderate Al_2O_3 (11.22 wt.% - 14.64 wt.%), a decrease in K_2O (1.87 wt.% - 4.07 wt.%) FeOt (1.46 wt.% - 1.68 wt.%), CaO (0.15 wt.% - 0.78 wt.%), P_2O_5 (0.06 wt.% - 0.07 wt.%), low TiO_2 (0.07 wt.% - 0.11 wt.%), MgO (0.05 wt.% - 0.17 wt.%), and MnO (0.09 wt.% - 0.12 wt.%) and LOI (0.3 wt.% - 1.3 wt.%). They display moderate Na_2O (3.86 wt.% - 4.98 wt.%) content, $K_2O + Na_2O$ (6.85 wt.% - 8.04 wt.%) and low K_2O/Na_2O ratios (0.38 wt.% - 1.05 wt.%). The fault rock-sulphidized sample is characterized by high SO_3 content (1.352 wt.%)m low silica content (64.88 wt.%), Al_2O_3 (14.75 wt.%), but displays an increase in FeOt (6.09 wt.%). Low K_2O (2.59 wt.%), CaO (1.16 wt.%), slight increase in TiO_2 (0.59 wt.%), MgO (2.16 wt.%), and MnO (0.33 wt.%). P_2O_5 (0.14 wt.%). They also display low K_2O/Na_2O ratios (0.62 wt.%), and $K_2O + Na_2O$ (6.80 wt.%), and subtle increase in LOI values from 2.3 wt.%. Fault rock-K-feldspar samples are characterized by a moderate silica content (73.62 wt.% - 74.96 wt.%). Low Al_2O_3 (12.69 wt.% - 13.5 wt.%), FeOt (2.15 wt.% - 2.3 wt.%), CaO (0.5 wt.% - 0.77 wt.%) TiO_2 (0.28 wt.% - 0.29 wt.%), MgO (0.29 wt.% - 0.42 wt.%), MnO (0.04 wt.% - 0.06 wt.%), P_2O_5 (0.05 wt.%) and LOI value (0.4) are also observed. The Na_2O content is more or less constant (3.5 wt.%), with a slight increase in K_2O/Na_2O ratios (1.45 wt.% - 1.53 wt.%), and $K_2O + Na_2O$ (8.59 wt.% - 8.96 wt.%).

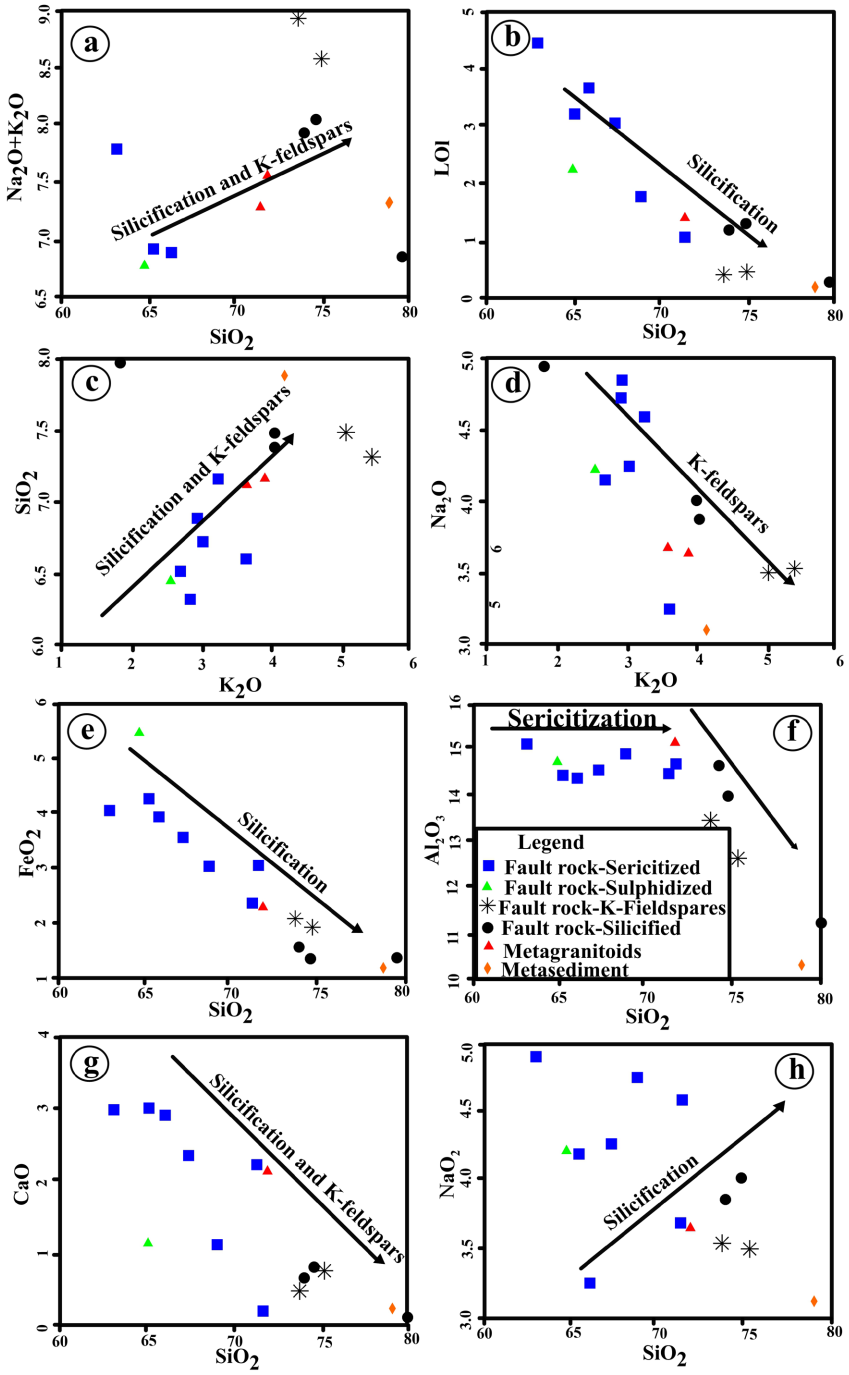

Figure 10. Harker diagrams showing variation of selected elements with silica.

The Least altered metasediment (CMRB-37) is characterized by a high silica content (78.88 wt.%) and moderate K_2O (4.2 wt.%). It displays a low Al_2O_3 (10.35 wt.%), Na_2O (3.12 wt.%) CaO (0.25 wt.%), P_2O_5 (0.01 wt.%), FeOt (1.31 wt.%), MgO (0.04 wt.%), TiO_2 (0.1), MnO (0.04 wt.%), K_2O/Na_2O ratios (0.99 wt.%), and LOI value of 0.2 wt.%.

Major element variations plot is presented in Figures 9(a)-(h), $Na_2O + K_2O$, K_2O and Na_2O show a positive correlation with SiO_2, while LOI, FeOt, CaO, and

Al_2O_3 decrease in concentration with increase in SiO_2. Na_2O also decreases with increase in K_2O. Al_2O_3 concentration is constant with sericitization, whereas sulphidation displays and increase in FeOt content.

4.2.2. Trace Element Composition

Fault rock-silicified samples display Au content of 0.6 ppb, with higher Au concentrations of 1.8 ppb observed in fault rock **s**ulphidized. These sulphidized samples with distinct ductile deformation features have the highest gold content and suggest that the domains with ductile deformation largely at the center of the shear zone are more prospective for gold: Invariably the brittle features are less endowed with gold. Sulphidation is mark by an increase in the transition trace elements (Cu, V, Mn, Co, Ni, Sc and Pb) alongside Au (Table 1). Some selected elements concentrations of the fault rocks were normalized to the average least altered metagranites in the Gankoumbol-Djouzami-Beka area (Figure 11). Enrichment peaks observed in Mn, Cu, S, Au, Te, Fe, Bi, Ba, Mo, Mg, and LREE (La, Sr). Ca, As, Sb, Ga, Cs, Sn and Nb are depleted. Generally, the concentration of Mn, and Ba is higher in the fault rock sulphidized, fault rock sericitized and fault rock silicified samples compared to the fault rock K-feldspars (Table 1). The Mn and Ba content is least in the least altered metagranitoids and metasediments. Sr concentration is high in fault rock sulphidized and fault rock sericitized compared to fault rock silicified, fault rock K-feldspars, least altered metagranitoids and metasediments. Sulphidation, silicification and sericitization are associated with increased in base metals Mn, Sr, Ba and Au. On the other hand, Zn concentration is high in the least altered metagranitoids compared to the altered fault rocks.

On the variation plots of selected element concentration with Au for both least altered and altered fault rocks, S, Cu, Fe, Mn, As, Te, Ni and Ba show a positive correlation with gold in the sulphidation zone (Figures 11(a)-(f)). Fault rock-sericitized shows a constant concentration with gold mineralization.

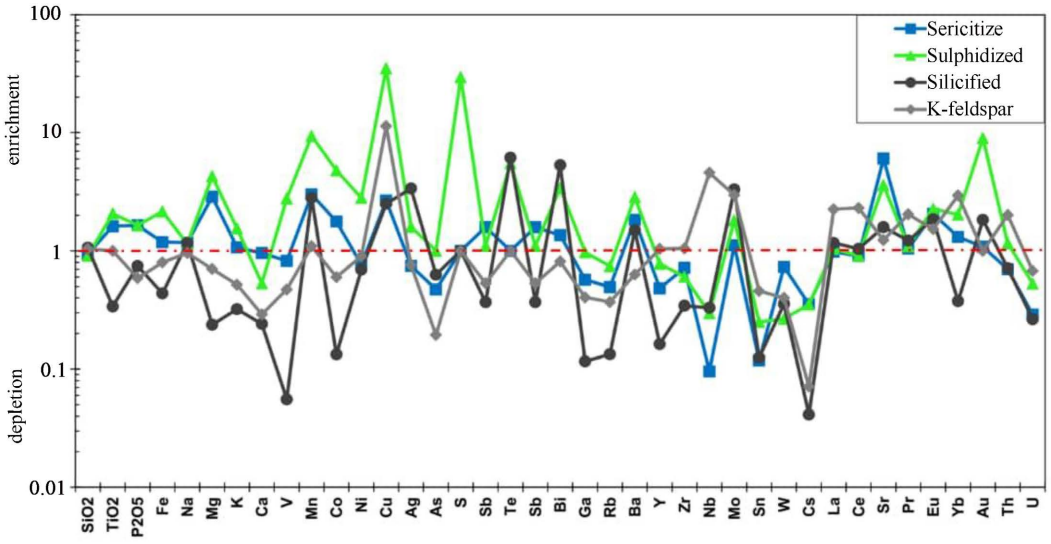

Figure 11. Depletion-enrichment diagram for selected elemental concentration for fault rocks relative in the GDB area.

On the C1 chondrite-normalized REE plot of [45], the samples show LREEs enrichment (CeN/SmN: 1.98 - 7.45, LaN/YbN: 4.17 - 51.81) and HREEs depletion (GdN/YbN: 1.19-6.84), with a strong to weak negative Eu anomaly (0.79 - 0.04; **Figure 10(a)**) a positive Ce anomaly and ΣREE = 30.7 - 103.2 ppm. On the multi-element variation plot (**Figure 10(b)**) normalized to values of [46], the least altered metagranitoi display peaks at Cs, U, Ce, Nd, Sm and Dy, with depletions in Nb, Ba, P, Ti and Zr. The metasediment displays peaks at Rb, Th, Nd, Ce, Pr and Dy, with depletions in Ba, Sr, Zr, Ti, Ta and Cs. The fault rocks display peaks at Th, La, Nd, U and Pr, with negative Nb, Zr, Ti, P and Ba. Fault rock-K-feldspar and Fault rock-sericitized samples display peaks at Rb and Sm and depletion in Sr compared to the other fault rocks. Fault rock-sulphidized sample displays peak in Dy.

5. Interpretation and Discussion

5.1. Petrological Analyses of the Auriferous Small-Scale Shear Zone in the Granitoid

The small-scale Gankoumbol-Djouzami-Beka shear zone (GDBSZ) is about 400 m wide (**Figure 2**). It is a typical brittle-ductile deformation zone with moderate to weak foliated low-strain fabrics towards the rims and strongly foliated higher-strain mylonitic/ultramylonitic zones at the center. It extends over several km along the NE-SW strike, straddling the boundary between the basement metasediments and the Pan African granitoids, and constitutes a segment of the CCSZ. The presence of both ductile and brittle structures (**Figures 3(a)-(f)**) within the investigated shear zone attests to the fact that the studied shear zone was developed at the brittle-ductile shear transition [11] [28]. Also, the presence of shear sense indicators depicting both sinistral and dextral sense of movement (**Figure 3** and **Figure 7**) is suggestive of the fact that the GDBSZ is characterized by polyphase deformation from D1-D4 [2] [12] [47]. The sinistral shear is dominant, with prolate type of strain ellipsoid, depicting deformation by constriction in a transtensional regime. The association of sinistral shear sense indicators with pyrite (sulphidation) at the microscopic scale (**Figures 7(a)-(c)**) may be suggestive of the fact that primary gold mineralization in the Upper Lom basin was initiated by sinistral shear movement. The NE-SW trending foliations together with sub-horizontal lineation characterized a strike-slip shear zone in a transtensional regime during the Pan-African tectonic evolution [2]. Grain size reduction from rim to core characterizes the shear zones [48], with coarse-grained least deformed metagranite (**Figures 4(b)-(c)**), grading to extremely deformed fine-grained foliated ultramylonite at the core (**Figure 5**). Furthermore, the development of a shear zone does not occur under-closed system conditions. Introducing or expelling fluids and mass during deformation has mineralogical consequences that control the rheology and the way the shear zone evolves. Fractures and lithological contacts (metagranitoid-metasediment interphase) represent pre-existing weaknesses that act as a site for shear zone nucleation and development. These structures also act

as conduits for fast fluid flow, catalyzing metamorphic and metasomatic growth phases, allowing the propagation and development of shear zone via a physical-chemical feedback mechanism [49]. Shear zones began as discrete structures from nucleation on fractures, widening due to wallrock weakening given the abundant evidence of fluid flow and syntectonic metamorphism [49]. This interpretation is consistent with that of the present study.

Shear sense indicators are well developed in high strain zones (**Figure 3** and **Figure 7**). Shear sense reversal in brittle-ductile regime associated with the collisional strike-slip tectonic setting may result from multiple senses of shear movement within a single deformation phase, or reorientation of principal stress axes thereby imposing an orthogonal switch on the principal orientation [49]. However, shear sense reversal within the Lom Basin, is attributed to polyphase deformation from D1-D4 [2] [12] in a transtensional regime during the Pan African Orogenic Belt evolution. This interpretation is consistent with that of this study. The healed fractures within the feldspars depict sub-magmatic deformations (**Figure 6(f)**), and evidence that pluton emplacement was synchronous with the deformation event. The shearing and dynamic recrystallization of quartz and feldspars with etch-surfaces regarded as dissolution textures (**Figure 6(b)** and **Figure 6(f)**) probably occurred under hydrous conditions as confirmed by previous researchers [50]. The infiltration of fluids was a key contributor to the localization of strain along the fracture planes, and shear zones developed through a chemical and mechanical transformation of the anhydrous coarse-grained host.

5.2. Geochemical Footprints of Alteration

Hydrothermal alteration is common in lode gold deposits and act as chemical traps for metal precipitation through water-rock interaction, and are generally favorable for mineralization [51] [52]. In hydrothermal ore deposits, alterations and metasomatism of parent rocks are crucial processes, because they record the details of ore formation through dissolution-reprecipitation mechanism. Alteration zones also mark the sharp interface between unaltered and altered mineralized zones. Gold mineralization associated with intense wallrock alteration is more or less structurally controlled [11] [53]. Sericitization, K-feldspar alteration, silicification and sulphidation constitute the alteration assemblages within the shear zone (**Figure 5** and **Figure 6**). These alteration assemblages trend NE-SW, defining the mineralogical-geochemical footprint towards Au mineralization. The hydrothermal alteration envelope shows some geochemical distinction from the least altered rocks to altered fault rocks. Diffusive sericitization is pervasive across the fault zone, with intensity increasing towards the ultramylonite/mylonite zone. Silicification is depicted by the high SiO_2 content (79.83 wt.%), low K_2O, CaO, P_2O_3 and LOI (**Table 1**) resulting from the introduction of secondary silica into the system and the replacement of former igneous and secondary minerals by quartz [45]. However, the abundance of quartz in brittle-ductile zones indicates the presence of hydrothermal fluids saturated in silica [8]. Sulphidation is marked

by an increased in S, Au and transition trace elements such as FeOt, Cu, Mn, Ni, Co, Cr, V, and Sr is attributed to sulphidization in the fault rocks [45], and occurrence of disseminated sulphides associated with Au mineralization (**Figure 6(b)** and **Figure 6(f)**). The Au content in this zone reaches a high of 1.8 ppb (**Table 1**). The low K_2O content in the Fault rock-sericitized is as a result of less K-feldspars, as sericite growth (sericitization) at the expense of K-feldspars. The slight Rb and Pb enrichments might be due to their preferential substitution for K^+ and Na^+ in the lattice of K-feldspar and sericite in the altered fault rocks during sericitization. The high concentration of Mn, Sr and Ba in the altered fault rocks depicts increasing hydrothermal alteration associated with Au mineralization. The high concentration of Zn in the least altered matagranitoids depicts a decrease in hydrothermal alteration.

Generally, the LOI content increases from the least altered samples (metagranite and metasediment) to altered fault rocks (**Table 1**, **Figure 4(b)**) as alteration intensity increased, forming massive sericite and muscovite (**Figure 5(e)**). The concentration of Na_2O remained almost constant across the fault rocks resulting from partial consumption of feldspars such as albite [53], indicating limited albitization (**Figure 10**). Al_2O_3 content varied slightly (10.36 - 15.2) for the sampled fault rocks due to its immobility, suggesting maybe a slight change in ore-bearing fluid source, from under saturated to Al saturated fluids. The low Al_2O_3 content in the metasediments may be suggestive of the fact that the Al-rich fluids were derived from a granitic source [46].

The predominant SiO_2 content in the major element concentration for the analyzed samples with concentrations ranging from (64.88 to 79.83 wt.%) is suggestive of a felsic source of the mineralizing fluids in the study [54]. The complex behavior of HFSE is seen in enrichment of Th, U and depletion of Nb and Ti. The negative Nb, Zr and Ti anomaly observed in the altered rocks is supportive of the breakdown/consumption of accessory zircon and titanite during alteration [45]; **Figure 12(b)**, or maybe indicating a higher immobility of HREEs during fluid-rock interactions. The studied samples show LREE enrichment relative to the HREE and a negative Eu anomaly reflecting plagioclase fractionation [55], and a reducing condition of mineralizing fluid (**Figure 12(a)**). The relatively low ΣREE content (**Table 1**) in the studied fault rocks points to the fact that the REE bearing minerals such as zircon, monazite, and apatite were gradually consumed as alteration intensity increased with fluid fluxes, from K-feldspar alteration through silicification to sericitization [53]. Also, the lack of secondary minerals to accommodate the REE or limited complex ligands like SO_4^{2-}, Cl^- and F^- to transport them may have contributed to their low concentrations. Sericitization, silicification provided suitable chemical traps, promoting Au mineralization through sulphidation, and is proposed to be the main mechanism for gold precipitation in orogenic gold deposit systems [11] [18]-[20] [28]. The Neoproterozoic granitoids described in the eastern goldfields in Cameroon are geochemically characterized as I-type, metaluminous to weakly peraluminous and calc-alkaline to shoshonitic,

associated with gold mineralization along wallrock alteration zones and in auriferous hydrothermal quartz veins (**Figure 9**; [11] [16]-[21]). Gold mineralization in GDB area within the Upper Lom Series is shear zone and intrusion-related, with hydrothermal alteration controlling the mineralization. The significant enrichment of base metals Cu, Mn, Te, S, Bi; Sr, Mg and Au in fault rock sulphidized is suggestive of their significant role in gold mineralization in the GDB area. The enrichment of base metals Au-S-Cu-Mn-Te-Fe-Mo-Bi alongside gold in the fault rock goes to supports the influence of a postmagmatic fluid responsible for concentrating gold [18].

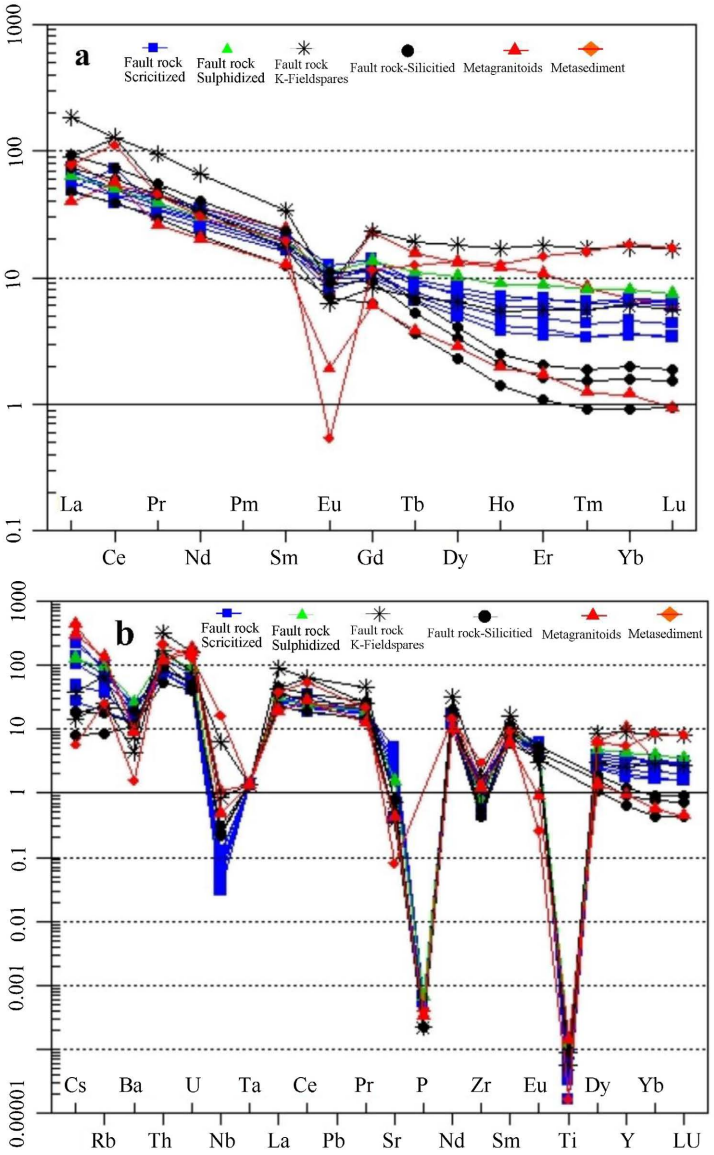

Figure 12. (a) Gankoumbol-Djouzami-Beka metagranitoids, metasediments and fault rock Chondrite-normalized REE patterns [43]; (b) Multielement variation patterns for the various alteration categories normalized to primitive mantle values of [44]. Note the strong negative Eu anomaly in least altered metagranite, metasediments and fault rock sulphidized. Fault rock silicified, sericitized and k-feldspar depict weak negative Eu anomaly.

5.3. Implications to Exploration

Shear zones act as deep major channels that serve as conduits for hydrothermal ore-forming fluid circulation. Ore bodies are mostly associated with second and third-order fractures along shear zones [7] [11]. The role of a shear zone in gold mineralization has been emphasized in different structural settings, where mineralization is coeval with deformation, magmatism, shearing, fluid-rock interaction, and hydrothermal alteration [56]. The brecciated nature of the studied rocks in the GDB area provided a suitable pathway for hydrothermal fluid circulation and favorable conditions for intense hydrothermal alteration and precipitation of gold. Such features have been proven to exhibit great potentials for disseminated ores. Shear zones at the granitoid-metasediment contact are major structures with good prospects for hydrothermal gold mineralization. This interpretation is consistent with field and geochemical data from the GDB area in the Upper Lom Basin, with strongly altered fault rocks as a potential host of gold along the shear zone in the eastern goldfield in Cameroon. Future exploration in the Upper Lom Series should target altered fault rocks along contact granitoids. Therefore, the possibilities of locating economic low-grade lode gold concentrations in the area are high, considering that intensive eluvial/alluvial gold workings are ongoing in the area. Hydrothermal alteration processes, therefore, remain the main gold enrichment determining factor, remobilizing gold in early magmatic sulphide minerals into favourable fracture-controlled zones by post-hydrothermal fluids dominated by sericitization, silicification, and sulphidation alteration. The role of hydrothermal activity in gold precipitation in this area is in line with previous fluid inclusion and isotopic data [19]. These data show that the fluid is carbonic from metamorphic devolatization and the stable oxygen and carbon isotope data are tied to fluid derivation from magmatic and metamorphic sources with unmixing playing a role in Au precipitation. This could be a powerful enrichment process in shear-zone-related granitoids in SE Cameroon [11] [18] [19]. Geochemical indicators such as enrichment and depletion patterns and geochemical pathfinder assemblage from factor analysis can provide key exploration information enabling Au vectoring in target areas. Granitoids in orogenic systems acted as rheological competent rock units, undergoing brittle-ductile deformation and forming suitable structural controls (shear zones) which acted as fluid pathways propagating hydrothermal alteration/mineralization [8] [57].

6. Conclusions

The following conclusion can be drawn from this study, based on the data presented here:

1) The GDBSZ is characterized by grain size reduction from the coarse grained less foliated low strain metagranitoid at the rims to the fine-grained, strongly foliated high-strain ultramylonite/mylonite at the center of the shear zone developed at the brittle-ductile transition. The extensively brecciated/fractured nature of host lithology in this shear zone points to the fact that deformation was syn-

chronous with strain localization and shear zone development via a physical-chemical feedback mechanism. The investigated shear zone was probably developed at the brittle-ductile transition, with sinistral and dextral shear sense indicators suggesting polyphase deformation from D1-D4.

2) Gold mineralization in the GDB area in the Upper Lom Basin occurs as disseminations in gold-bearing quartz veins, and as metasomatic-hydrothermal replacement gold at the granitoid-metasediment contact, with alteration zone hosting 0.6 - 1.8g/t Au.

3) Au-Cu-S-Fe-Mn-Te-Se defines the pathfinder assemblage emerging depletion/enrichment plots. The mineralization is associated with major lithology, hydrothermal alteration and sulphidation, suggesting that gold mineralization was synchronous with shear zone formation. The enrichments and depletions elucidated by geochemical data constitute the geochemical footprint in GDB area. Hydrothermal alteration processes, therefore, remain the main gold enrichment determining factor, remobilizing gold in early magmatic sulphide minerals into favorable micro-shear, fault zone, and fracture-controlled zones by post-hydrothermal fluids dominated by sericitization, silicification, and sulphidation alteration.

Highlights

1) The Gankoumbol-Djouzami-Beka shear zone (GDBSZ) is a typical brittle-ductile deformation zone.

2) It shows a characteristic moderate to weak foliated fabrics towards the rims and strongly foliated ultramylonitic zones at the center.

3) Sinistral shear sense indicators are associated with gold mineralization depicted by sulphidation, silicification and sericitization.

4) Hydrothermal alteration processes, remain the main gold enrichment determining factor.

Conflicts of Interest

The authors have no relevant financial or nonfinancial interests to disclose.

References

[1] Ngako, V., Affaton, P. and Njonfang, E. (2008) Pan-African Tectonics in Northwestern Cameroon: Implication for the History of Western Gondwana. *Gondwana Research*, **14**, 509-522. https://doi.org/10.1016/j.gr.2008.02.002

[2] Kankeu, B., Greiling, R.O. and Nzenti, J.P. (2009) Pan-African Strike-Slip Tectonics in Eastern Cameroon-Magnetic Fabrics (AMS) and Structure in the Lom Basin and Its Gneissic Basement. *Precambrian Research*, **174**, 258-272. https://doi.org/10.1016/j.precamres.2009.08.001

[3] de Lira Santos, L.C.M. and Viegas, L.G.F. (2021) Exploring the Relationships between Shear Zones and Granites: Field and Microstructural Data for Contrasting Case Studies of the Borborema Province (NE do Brazil). *Geologia USP. Série Científica*, **21**, 3-18. https://doi.org/10.11606/issn.2316-9095.v21-180579

[4] Fossen, H. and Cavalcante, G.C.G. (2017) Shear Zones—A Review. *Earth-Science Re-*

views, **171**, 434-455. https://doi.org/10.1016/j.earscirev.2017.05.002

[5] Groves, D.I., Santosh, M., Goldfarb, R.J. and Zhang, L. (2018) Structural Geometry of Orogenic Gold Deposits: Implications for Exploration of World-Class and Giant Deposits. *Geoscience Frontiers*, **9**, 1163-1177. https://doi.org/10.1016/j.gsf.2018.01.006

[6] Goldfarb, R.J., Groves, D.I. and Gardoll, S. (2001) Orogenic Gold and Geologic Time: A Global Synthesis. *Ore Geology Reviews*, **18**, 1-75. https://doi.org/10.1016/s0169-1368(01)00016-6

[7] Cheng, N., Hou, Q., Shi, M., He, M., Liu, Q., Yan, F., *et al.* (2019) New Insight into the Genetic Mechanism of Shear Zone Type Gold Deposits from Muping-Rushan Metallogenic Belt (Jiaodong Peninsula of Eastern China). *Minerals*, **9**, Article 775. https://doi.org/10.3390/min9120775

[8] Suh, C.E. and Dada, S.S. (1997) Fault Rocks and Differential Reactivity of Minerals in the Kanawa Violaine Uraniferous Vein, NE Nigeria. *Journal of Structural Geology*, **19**, 1037-1044. https://doi.org/10.1016/s0191-8141(97)00010-2

[9] Caby, R., Sial, A.N., Arthaud, M. and Vauchez, A. (1991) Crustal Evolution and the Brasiliano Orogeny in Northeast Brazil. In: Dallmeyer, R.D. and Lécorché, J.P., Eds., *The West African Orogens and Circum-Atlantic Correlatives*, Springer Berlin Heidelberg, 373-397. https://doi.org/10.1007/978-3-642-84153-8_16

[10] Toteu, S.F., Penaye, J. and Djomani, Y.P. (2004) Geodynamic Evolution of the Pan-African Belt in Central Africa with Special Reference to Cameroon. *Canadian Journal of Earth Sciences*, **41**, 73-85. https://doi.org/10.1139/e03-079

[11] Suh, C.E., Lehmann, B. and Mafany, G.T. (2006) Geology and Geochemical Aspects of Lode Gold Mineralization at Dimako-Mboscorro, SE Cameroon. *Geochemistry: Exploration, Environment, Analysis*, **6**, 295-309. https://doi.org/10.1144/1467-7873/06-110

[12] Ngako, V., Affaton, P., Nnange, J.M. and Njanko, T. (2003) Pan-African Tectonic Evolution in Central and Southern Cameroon: Transpression and Transtension during Sinistral Shear Movements. *Journal of African Earth Sciences*, **36**, 207-214. https://doi.org/10.1016/s0899-5362(03)00023-x

[13] Njanko, T., Nédélec, A., Kwékam, M., Siqueira, R. and Esteban, L. (2010) Emplacement and Deformation of the Fomopéa Pluton: Implication for the Pan-African History of Western Cameroon. *Journal of Structural Geology*, **32**, 306-320. https://doi.org/10.1016/j.jsg.2009.12.007

[14] Fon, A.N., Suh, C.E., Vishiti, A., Ngatcha, R.B., Ngang, T.C., Shemang, E.M., *et al.* (2021) Gold Dispersion in Tropical Weathering Profiles at the Belikombone Gold Anomaly (Bétaré Oya Gold District), East Cameroon. *Geochemistry*, **81**, Article 125770. https://doi.org/10.1016/j.chemer.2021.125770

[15] Ntieche, B., Nguet, P.W., Nchouwet, Z., Mounjouohou, M.A. and Mfepat, D. (2020) Deformation Features and Structures in Some Igneous and Metamorphic Rocks: A Case Study of Central African Fold Belt in Cameroon. https://www.intechopen.com/chapters/72765

[16] Asaah, A.V., Zoheir, B., Lehmann, B., Frei, D., Burgess, R. and Suh, C.E. (2014) Geochemistry and Geochronology of the ~620 Ma Gold-Associated Batouri Granitoids, Cameroon. *International Geology Review*, **57**, 1485-1509. https://doi.org/10.1080/00206814.2014.951003

[17] Ateh, K.I., Suh, C.E., Shemang, E.M., Vishiti, A., Tata, E. and Chombong, N.N. (2017) New LA-ICP-MS U-Pb ages, Lu-Hf Systematics and REE Characterization of Zircons from a Granitic Pluton in the BétaréOya Gold District, SE Cameroon. *Journal of Ge-*

oscience and Geomatics, **5**, 267-283.

[18] Ngatcha, R.B., Okunlola, O.A., Suh, C.E., Ateh, K.I. and Hofmann, A. (2019) Petrochemical Characterization of Neoproterozoic Colomine Granitoids, SE Cameroon: Implications for Gold Mineralization. *Lithos*, **344-345**, 175-192. https://doi.org/10.1016/j.lithos.2019.06.028

[19] Ndonfack, A.K.I., Xie, Y. and Goldfarb, R. (2021) Gold Occurrences of the Woumbou-Colomine-Kette District, Eastern Cameroon: Ore-Forming Constraints from Petrography, SEM-CL Imagery, Fluid Inclusions, and C-O-H-S Isotopes. *Mineralium Deposita*, **57**, 83-105.

[20] Tata, E., Suh, C.E., Vishiti, A., Shemang, E.M., Fon, A.N., Ateh, K.I., *et al.* (2018) Wallrock Alteration Categories and Their Geochemical Signatures in Gold-Bearing Neoproterozoic Granitoids, Batouri Gold District, Southeastern Cameroon. *Geochemistry: Exploration, Environment, Analysis*, **19**, 269-288. https://doi.org/10.1144/geea2016-017

[21] Vishiti, A., Suh, C.E., Lehmann, B., Egbe, J.A. and Shemang, E.M. (2015) Gold Grade Variation and Particle Microchemistry in Exploration Pits of the Batouri Gold District, SE Cameroon. *Journal of African Earth Sciences*, **111**, 1-13. https://doi.org/10.1016/j.jafrearsci.2015.07.010

[22] Nzenti, J.P., Kapajika, B., Wörner, G. and Lubala, T.R. (2006) Synkinematic Emplacement of Granitoids in a Pan-African Shear Zone in Central Cameroon. *Journal of African Earth Sciences*, **45**, 74-86. https://doi.org/10.1016/j.jafrearsci.2006.01.005

[23] Liégeois, J., Abdelsalam, M.G., Ennih, N. and Ouabadi, A. (2013) Metacraton: Nature, Genesis and Behavior. *Gondwana Research*, **23**, 220-237. https://doi.org/10.1016/j.gr.2012.02.016

[24] Toteu, S.F., Van Schmus, W.R. and Penaye, J. (2006) The Precambrian of Central Africa. *Journal of African Earth Sciences*, **44**, 7-10. https://doi.org/10.1016/j.jafrearsci.2005.12.003

[25] Tchameni, R., Pouclet, A., Penaye, J., Ganwa, A.A. and Toteu, S.F. (2006) Petrography and Geochemistry of the Ngaoundéré Pan-African Granitoids in Central North Cameroon: Implications for Their Sources and Geological Setting. *Journal of African Earth Sciences*, **44**, 511-529. https://doi.org/10.1016/j.jafrearsci.2005.11.017

[26] Nomo, E.N., Tchameni, R., Vanderhaeghe, O., Sun, F., Barbey, P., Tekoum, L., *et al.* (2017) Structure and LA-ICP-MS Zircon U-Pb Dating of Syntectonic Plutons Emplaced in the Pan-African Banyo-Tcholliré Shear Zone (Central North Cameroon). *Journal of African Earth Sciences*, **131**, 251-271. https://doi.org/10.1016/j.jafrearsci.2017.04.002

[27] Gazel, J. and Gérard, G. (1954) Carte géologique de reconnaissance du cameroun au 1:500,000, feuille batouri Est avec notice explicative. memoire direction mines géologie, Yaoundé, Cameroon.

[28] Suh, C.E. (2008) Sulphide Microchemistry and Hydrothermal Fluid Evolution in Quartz Veins, Batouri Gold District (Southeast Cameroon). *Journal of the Cameroon Academy of Science*, **8**, 19-30.

[29] Vishiti, A., Suh, C.E., Lehmann, B., Shemang, E.M., Ngome, N.L.J., Nshanji, N.J., *et al.* (2017) Mineral Chemistry, Bulk Rock Geochemistry, and S-Isotope Signature of Lode-gold Mineralization in the Bétaré Oya Gold District, South-East Cameroon. *Geological Journal*, **53**, 2579-2596. https://doi.org/10.1002/gj.3093

[30] Takodjou Wambo, J.D., Pour, A.B., Ganno, S., Asimow, P.D., Zoheir, B., Salles, R.d.R., *et al.* (2020) Identifying High Potential Zones of Gold Mineralization in a Sub-Tropical Region Using Landsat-8 and ASTER Remote Sensing Data: A Case Study of

the Ngoura-Colomines Goldfield, Eastern Cameroon. *Ore Geology Reviews*, **122**, Article 103530. https://doi.org/10.1016/j.oregeorev.2020.103530

[31] Ngatcha, R.B., Suh, C.E., Okunlola, O.A., Nunoo, S., Ateh, K.I., Elburg, M. and Hofmann, A. (2021) Crustal Modelling from Pan-African granites of the Colomine Gold District, SE Cameroon: Insights from zircon U-Pb dating and Lu-Hf Isotope Systematics. *Journal of African Earth Sciences*, 104441.

[32] Milesi, J.P., Toteu, S.F., Deschamps, Y., Feybesse, J.L., Lerouge, C., Cocherie, A., *et al.* (2006) An Overview of the Geology and Major Ore Deposits of Central Africa: Explanatory Note for the 1:4,000,000 Map "Geology and Major Ore Deposits of Central Africa". *Journal of African Earth Sciences*, **44**, 571-595. https://doi.org/10.1016/j.jafrearsci.2005.10.016

[33] Soba, D., Michard, A., Toteu, S.F., Norman, D.I., Penaye, J., Ngako, V., *et al.* (1991) U-Pb, SM-Nd and Rb-Sr Dating in the Pan African Mobile Belt of Eastern Cameroon: Upper Proterozoic Age of the Lom Series. *Comptes Rendus de L¨ Academie des Sciences*, **312**, 1453-1458.

[34] Passchier, C.W. and Trouw, R.A.J. (2005) Microtectonics. Springer.

[35] Passchier, C.W. and Trouw, R.A.J. (1998) Deformation Mechanisms: In: Microtectonics. Springer, https://10.1007/978-3-662-08734_3.

[36] Ramsay, J.G. (1967) Folding and Fracturing of Rocks. MacGraw-Hill. 568 p.

[37] Lisle, R. (1977) Estimation of the Tectonic Strain Ratio from the Mean Shape of Deformed Elliptical Objects. *Geologie en Mijnbouw*, **56**, 140-144.

[38] Ragan, D.M. (1973) Structural Geology: An Introduction to Geometrical Techniques. 2nd Edition, John Wiley and Sons, 1-208.

[39] Cox, K.G., Bell, J.D. and Pankhurst, R.J. (1979) The Interpretation of Igneous Rocks. George Allen & Unwin.

[40] Shand, S.J. (1943) Eruptive Rocks. Their Genesis, Composition, Classification, and Their Relation to Ore-Deposits with a Chapter on Meteorite. John Wiley & Sons.

[41] Pearce, J.A., Harris, N.B.W. and Tindle, A.G. (1984) Trace Element Discrimination Diagrams for the Tectonic Interpretation of Granitic Rocks. *Journal of Petrology*, **25**, 956-983. https://doi.org/10.1093/petrology/25.4.956

[42] Peccerillo, A. and Taylor, S.R. (1976) Geochemistry of Eocene Calc-Alkaline Volcanic Rocks from the Kastamonu Area, Northern Turkey. *Contributions to Mineralogy and Petrology*, **58**, 63-81. https://doi.org/10.1007/bf00384745

[43] Boynton, W.V. (1984) Cosmochemistry of the Rare Earth Elements: Meteorite Studies. In: *Developments in Geochemistry*, Elsevier, 63-114. https://doi.org/10.1016/b978-0-444-42148-7.50008-3

[44] McDonough, W.F. and Sun, S.-S. (1995) The Composition of the Earth. *Chemical Geology*, **120**, 223-253. https://doi.org/10.1016/0009-2541(94)00140-4

[45] Li, X., Fan, H., Santosh, M., Hu, F., Yang, K. and Lan, T. (2013) Hydrothermal Alteration Associated with Mesozoic Granite-Hosted Gold Mineralization at the Sanshandao Deposit, Jiaodong Gold Province, China. *Ore Geology Reviews*, **53**, 403-421. https://doi.org/10.1016/j.oregeorev.2013.01.020

[46] Fontem, N.K., Suh, C.E., Ngatcha, R.B., Shemang, E.M., Vishiti, A., Melchiorre, E., *et al.* (2023) Tourmaline Occurrence and Gold Mineralization at a Granitoid-Metasediment Contact in the Upper Lom Basin, East Cameroon. *SN Applied Sciences*, **5**, Article No. 141. https://doi.org/10.1007/s42452-023-05358-z

[47] Dutta, D. and Mukherjee, S. (2019) Opposite Shear Senses: Geneses, Global Occurrences, Numerical Simulations and a Case Study from the Indian Western Himalaya.

Journal of Structural Geology, **126**, 357-392. https://doi.org/10.1016/j.jsg.2019.05.008

[48] Cao, S., Zhan, L., Dong, Y. and Li, W. (2022) Strain Localized Deformation Variation of a Small-Scale Ductile Shear Zone. Solid Earth, EGU. Preprint. https://doi.org/10.5194/se-2022-2

[49] Condit, C.B. and Mahan, K.H. (2022) Fracturing, Fluid Flow, and Shear Zone Development: Relationships between Chemical and Mechanical Processes in Proterozoic mafic Dykes from Southwestern Montana, USA. *Journal of Metamorphic Geology*, **36**, 195-223.

[50] Parsons, A.J., Coleman, M.J., Ryan, J.J., Zagorevski, A., Joyce, N.L., Gibson, H.D., *et al.* (2018) Structural Evolution of a Crustal-Scale Shear Zone through a Decreasing Temperature Regime: The Yukon River Shear Zone, Yukon-Tanana Terrane, Northern Cordillera. *Lithosphere*, **10**, 760-782. https://doi.org/10.1130/l724.1

[51] Hastie, E.C.G., Kontak, D.J. and Lafrance, B. (2020) Gold Remobilization: Insights from Gold Deposits in the Archean Swayze Greenstone Belt, Abitibi Subprovince, Canada. *Economic Geology*, **115**, 241-277. https://doi.org/10.5382/econgeo.4709

[52] Ma, W., Deng, T., Xu, D., Chi, G., Li, Z., Zhou, Y., *et al.* (2021) Geological and Geochemical Characteristics of Hydrothermal Alteration in the Wangu Deposit in the Central Jiangnan Orogenic Belt and Implications for Gold Mineralization. *Ore Geology Reviews*, **139**, Article 104479. https://doi.org/10.1016/j.oregeorev.2021.104479

[53] Li, R., Albert, N.N., Yun, M., Meng, Y. and Du, H. (2019) Geological and Geochemical Characteristics of the Archean Basement-Hosted Gold Deposit in Pinglidian, Jiaodong Peninsula, Eastern China: Constraints on Auriferous Quartz-Vein Exploration. *Minerals*, **9**, Article 62. https://doi.org/10.3390/min9010062

[54] Djagre, L., Ali, K., Kra, L.K. and Koffi, B.G. (2025) Geological Controls on Gold Mineralization of the Nyangboué Prospect in the Southern Part of the Boundiali-Syama Belt, Northwest Ivory Coast. *Scientific African*, **27**, e02584. https://doi.org/10.1016/j.sciaf.2025.e02584

[55] Shirazi, M.S., Lotfi, M., Nezafati, N. and Gourabjiripour, A. (2021) Geology, Geochemistry, and Some Genetic Discussion of the IIC Anomaly, BAFQ District, Central Iran. *Revista Geoaraguaia*, **11**, 95-117.

[56] Tang, L. and Santosh, M. (2018) Neoarchean Granite-Greenstone Belts and Related Ore Mineralization in the North China Craton: An Overview. *Geoscience Frontiers*, **9**, 751-768. https://doi.org/10.1016/j.gsf.2017.04.002

[57] Chinnasamy, S.S. and Mishra, B. (2013) Greenstone Metamorphism, Hydrothermal Alteration, and Gold Mineralization in the Genetic Context of the Granodiorite-Hosted Gold Deposit at Jonnagiri, Eastern Dharwar Craton, India. *Economic Geology*, **108**, 1015-1036. https://doi.org/10.2113/econgeo.108.5.1015